# Analytical Methods

Accepted Manuscript


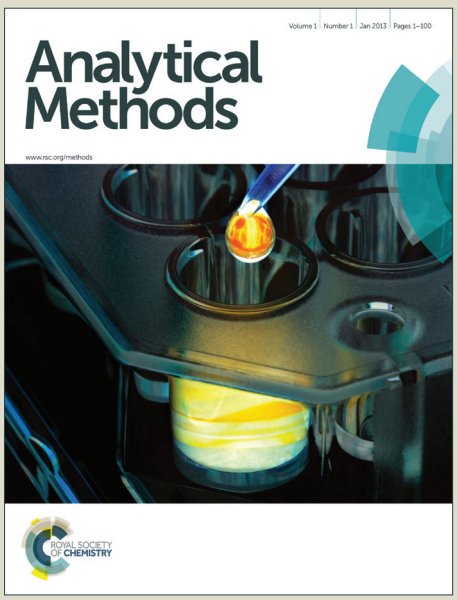





ROYAL SOCIETY OF CHEMISTRY

www.rsc.org/methods

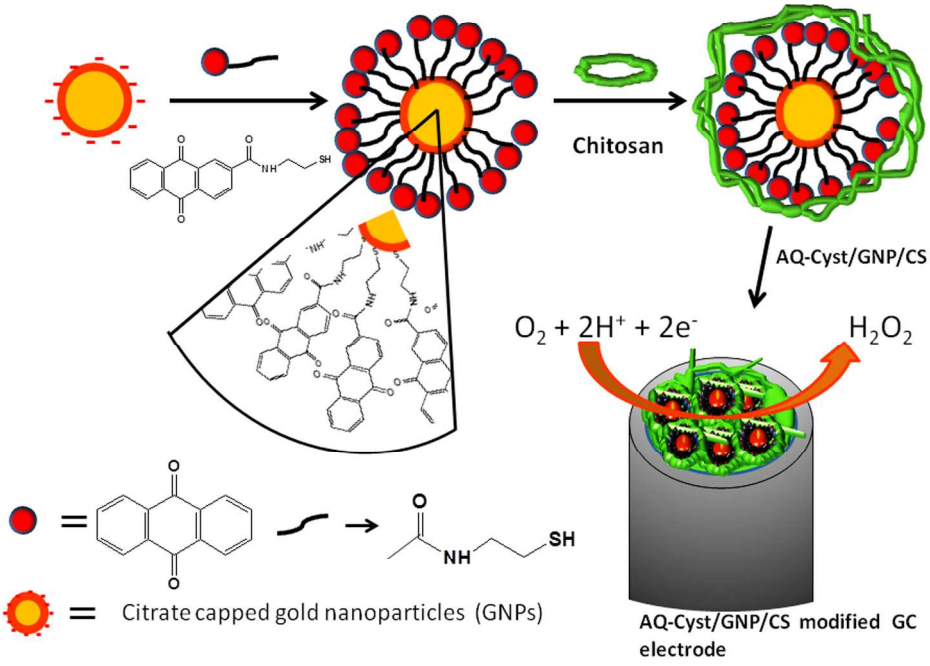


254x190mm (300 x 300 DPI)

# Anthraquinone moiety/cysteamine functionalized-gold nanoparticle/Chitosan based nanostructured composite for the electroanalytical detection of dissolved oxygen within aqueous media

Ida Tiwari [1]*, Mandakini Gupta[1], Rajiv Prakash[2], Craig E. Banks,[3]

*[1]Centre of Advanced Study in Chemistry, Faculty of Science, Banaras Hindu University, Varanasi (INDIA)*
*[2]School of Material Science and Technology, Indian Institute of Technology, Banaras Hindu University, Varanasi (INDIA)*
*[3]Faculty of Science and Engineering, School of Science and the Environment, Division of Chemistry and Environmental Science, Manchester Metropolitan University, Chester Street, Manchester, M15GD, Lancs., UK*

**Abstract:**

This work reports a nanostructured composite electrode comprising gold nanoparticles, anthraquinone derivatives and chitosan electrically wired via immobilisation upon a glassy carbon macroelectrode. The as-prepared nanostructured composite was morphologically characterised using transmission electron microscopy with surface characterization performed with atomic force microscopy while other physical characterization was undertaken by infra-red, UV-Vis, and energy dispersive X-ray spectroscopy. Electrochemical investigations and stability of the composite electrode was undertaken by cyclic voltammetry. Electrocatalytic activity of the composite electrode was investigated for the oxygen reduction reaction in 0.1 M phosphate buffer solution of pH 6.5. Furthermore, the response characteristics show that this fabricated electrode has a shelf-life of between 3 to 4 months and has improved electrochemical and electrical properties and firm adhesion of the material with homogeneous dispersion at the electrode surface. The linear range and detection limit for the electrochemical detection of dissolved oxygen in the optimum condition using the nanostructured composite was found to be over the accessible range of 0.2 to 5.8 mg $L^{-1}$ and 0.03 mg $L^{-1}$ respectively.

**Keywords:** Modified electrode; Gold nanoparticles; Anthraquinone derivatives; Nanocomposite

* Corresponding author:

Ida Tiwari:Tel: +91-9415813020; Fax: +91-542-2368174; *E-mail address:*idatiwari_2001@rediffmail.com

## 1. Introduction:

Nanostructured materials have been used to extensively prepare nanocomposites which have been applied in many diverse fields [1]. Nanocomposites refer to composites in which one of the phases has nanoscale morphology such as nanoparticles, nanotubes or lamellar nanostructure [2]. Nanocomposites have exceptionally high surface to volume ratios or high aspect ratios, hence have such geometric properties as compared to conventional composite materials making them suitable for a range of sensing applications [3]. Among these, metal nanoparticles such as colloidal gold nanoparticles possess unique chemical, extraordinary catalytic activity and electromagnetic properties which are strongly dependent on size, shape and surrounding environment of particles [4]. These unique properties of gold nanoparticles are mainly due to their high surface to volume ratio and high surface energy [5]. Chitosan is a natural polymer, made up of linear polysaccharide of β-(1-4)-linked D-glucosamine (deacetylated unit) and N-acetyl-D-glucosamine (acetylated unit) Poly-N-acetyl glucosamine and is obtained by deacetylation of natural polymer chitin which is the structural element of exoskeleton of crustaceans and cell wall of fungi [6]. Due to biodegradable and biocompatible nature of chitosan, it has been used in medical applications as surgical sutures, immunosuppressant and artificial skin [7, 8]. Consequently chitosan can be used as a matrix for the preparation of nanomaterial based polymer nanocomposite which can be beneficially applied in the field of sensors [9].

The electrocatalytic reduction of oxygen is an important reaction in the field of electrochemistry owing to its technological importance in many fields involving fuel cells, sensors, metal–air batteries, in the electrosynthetic production of hydrogen peroxide, medical applications, and some biochemical processes where the oxygen plays a key role, in the food production [10-12]. The electrochemical reduction of oxygen occurs mainly by two routes based on the electrode material and the solution composition. Two electron transfer involves

the production of hydrogen peroxide and four electron transfer results involve the production of water which is the characteristic reaction favoured in fuel cell applications [13]. In this connection, various modifiers have been used for the detection of dissolved oxygen, such as porphyrins [14,15], phenanthrenequinone [16] , bi-submonolayer-modified Au (III) surfaces [17], wired enzymes [18,19], manganese oxide nanoparticles [20], platinum nanoparticles [21,22], multiwalled carbon nanotubes [13,23,24], and diaminonaphthalene and glyoxalbis(2-hydroxyanil) metal complexes modified electrodes [25,26] to name just a few. Quinone based compounds such as anthraquinones and their derivatives can also act as redox mediator or an electrocatalyst for the oxygen reduction reaction as they possess several π-electrons and reducible p-quinone system which can involve in electron transfer reaction and decrease the overpotential required for activation [27]. Various reports are available for using anthraquinone and their derivatives as redox mediators for horseradish peroxidase in hydrogen peroxide sensor [28, 29] and oxygen reduction/dissolved oxygen detection [23, 27, 30-44]. The probable mechanism for the role of anthraquinone and their derivatives is reported to be as follows [45]:

Step (I): Formation of quinone radical anion

$$Q + e^- \rightarrow Q^{\bullet -}$$

Step (II): Formation of superoxide ion (Rate determining step)

$$Q^{\bullet -} + O_2 \xrightarrow{K_c} O_2^{\bullet -} + Q$$

Step (III): Disproportionation reaction

$$2O_2^{\bullet -} + H_2O \rightarrow O_2 + HO_2^- + OH^-$$

Or

Step (IV): Reduction of $O_2$ at the electrode

$$O_2^{\bullet -} + H_2O + e^- \rightarrow HO_2^- + OH^-$$

where Q denotes surface quinone species. Hence, the modification of electrodes with quinone moiety facilitates the electron transfer for the reduction of oxygen. Note that such approaches involve potential cycling to induce such groups or through modification with quinone type moieties. Although, anthraquinone and their derivatives have been used as redox active materials for the electrochemical reduction of oxygen, their electrochemistry is poor as large peak separations and diffused peaks are observed. Hence, it would be desirable to overcome this by using this mediator with nanomaterials which can improve the electrochemical performance of the sensor. Multiwalled carbon nanotubes [46-48] have been employed for this purpose by our group and promising results have been reported. Extending our work further for further improvements we have prepared a nanocomposite material using anthraquinone-2-COOH/ Cysteamine (AQ-Cyst) capped gold nanoparticles (GNPs) which act as a reinforcement element and chitosan (CS) which acts as a matrix material for dispersion of this prepared nanocomposite over the electrode. To the best of our knowledge, no reports are available reporting the use of GNPs with anthraquinone moieties for the electrochemical reduction of oxygen. Further, this AQ-Cyst/GNPs/CS nanocomposite has been used as the basis of a dissolved oxygen sensor.

## 2. Experimental:

### 2.1 Reagents and Materials:

Gold nanocomposites were prepared by the citrate fabrication method as previously reported [48]. Hydrogen trichloroauratetrihydrate ($HAuCl_4$) was purchased from Aldrich (USA). Anthraquinone-2-carboxylic acid (AQ-COOH), 1-ethyl-3-(3-dimethylaminopropyl) carbodiimide hydrochloride (EDC), N-hydroxysulfosuccinimide (NHS) and cysteamine were purchased from Sigma (USA). All other chemicals employed were of analytical grade. All the solutions were prepared with triple distilled water. All the experiments were performed in 0.1 M phosphate buffer solution (pH 6.5). CS was purchased from Sigma (USA; MW: 2.4 $x10^6$ Da) and CS solution was prepared by method as reported [49] and stored at $4^{\circ}$ C in a refrigerator when required. Pond water for real sample analysis was collected from pond of Botanical garden, Banaras Hindu University in sterilized plastic bottles and immediately used for analysis.

### 2.2 Instruments:

The electrochemical measurements were performed with CHI 630C series (USA) electrochemical system. Cyclic voltammetry studies were performed in electrochemical cell with three electrode system including modified glassy carbon electrode as a working electrode, an Ag/AgCl reference electrode and Pt wire as counter electrode using CHI 630 C series (USA) electrochemical instrument. All electrochemical measurements were carried out in 4 mL phosphate buffer solution, pH 6.5 and deaerated by bubbling pure nitrogen for at 15 minutes prior to the experiments and between measurements.

The UV-Vis spectroscopic measurement of an aqueous solution of AQ-COOH, AQ-Cysteamine (AQ-Cyst) composite system and AQ-Cyst functionalized GNPs nanocomposite

were performed with UV-Vis spectrophotometer (Hitachi, U-3900). AFM of the nanocomposite film was performed with Nanosurf Easyscan-2 AFM instrument by scanning with silicon tip (CONTR-10) in the contact static mode. TEM measurements of GNPs and AQ functionalized GNPs nanocomposite was performed on a TecnaiG2 instrument. The samples were dispersed in distilled water and deposited onto copper grid for TEM measurements. The particle size and zeta potential measurement of the prepared nanocomposite was performed using Dynamic light scattering (DLS) measurements in aqueous solution with a Zetasizer Nano-ZS90 (Malvern Instruments) at a scattering angle of $90^0$ and constant temperature of $25^0$C.

**2.3 Preparation of nanocomposite:**

**2.3.1. Preparation of GNPs:**

In a typical experiment, before preparation of GNPs, apparatus used was pre-cleaned in chromic acid solution. Then aqua regia *(3:1HCl/HNO$_3$)* was used for cleaning and finally, all the apparatus was thoroughly rinsed with distilled water. 5 mL of 1 mM of hydrogen trichloroaurate trihydrate solution was prepared in around bottom flask and was vigorously boiled with stirring, fitted with reflux condenser. Then 0.5 mL of sodium citrate (38.8 mM) was added quickly. The solution was refluxed for 15 minutes. The solution was cooled to room temperature and stirred continuously. The prepared GNPs were characterized using UV-Visible spectroscopy as discussed subsequently. The average size of the prepared GNPs was found to be 8-10 nm by transmission electron microscopy (TEM) analysis (Supplementary Material I).

**2.3.2 Preparation of AQ-Cyst complex and AQ-Cyst/GNPs nanocomposite:**

AQ-Cyst complex was prepared by carbodiimide coupling reaction process. In this process, 11.6 mg of AQ-COOH was suspended in 700 µL of HEPES [2-{4-(2-hydroxyethyl)

piperazin-1-yl} ethane sulfonic acid] buffer solution. To this solution, 44 mg of NHS and 60 mg of EDC were added. The solution was stirred for 45 minutes. 100 µL of cysteamine was added drop wise along with vigorous stirring and the mixture was left at room temperature for 24 hours. Conjugate was washed with water several times, centrifuged and dried in desiccators. Further, GNPs were added to AQ-Cyst complex and ultrasonication was done for 30 minute in a bath. The nanocomposite was washed with triple distilled water, filtered and dried and was further used for FTIR spectroscopy.

**2.3.3. Preparation of AQ-Cyst/GNPs/CS nanocomposite modified electrode:**

A glassy carbon electrode (GCE) was cleaned with alumina (0.5 µm), followed by ultrasonication in distilled water and was allowed to dry at room temperature. For the electrode modification, 20 µL GNPs solution (2 mM) was added to 10 mg/mL aqueous solution of AQ-Cyst complex, ultrasonicated in a water bath for 30 minutes, filtered and dried. This prepared AQ-Cys/GNPs nanocomposite was suspended in 1 mL CS matrix by ultrasonication in a water bath for 15 minutes. 5 µL of prepared AQ-Cyst/GNPs/CS nanocomposite solution was dropped on the pre-treated GCE and was allowed to dry at room temperature for 1 hour. The prepared electrode was washed with triple distilled water twice to remove non-adsorbed nanocomposite material. For optimization of GNPs concentration, different modified electrode were prepared by following same procedure with the varying amounts of GNPs solution (2 mM, 10, 20, 30, 40, 50 µL) and keeping the AQ-Cyst complex (10mg/mL aqueous solution each) and CS constant in different vials. Optimization study was performed by studying the electrochemistry of above electrodes by using cyclic voltammetry technique and the data has been shown as bar graph for subsequent electrodes (Supplementary material II).

## 3. Results and discussion:

### 3.1 Basic mechanism of covalent interaction of cysteamine with AQ-COOH:

To link cysteamine with AQ-COOH, EDC and NHS were used. EDC and NHS used for this reaction are classified as zero length cross-linking reagents because during cross-linking, atoms are eliminated from the reactants thus shortening the distance between the two linked moieties [50]. In this reaction, EDC activates the terminal –COOH groups of AQ-COOH forming a highly reactive O-acylurea active intermediate. Furthermore, the surface of O-acylurea transforms by nucleophilic attack of NHS to form succinimidyl ester with the release of urea as a byproduct. A subsequent nucleophilic attack by primary nitrogen of amino compound (cysteamine) to the succinimidyl ester brings about the formation of the amide linkage [51].

### 3.2. Modification of citrate–reduced GNPs with AQ-Cyst complex to form AQ-Cyst/GNPs nanocomposite:

Attention was turned in order to modify the citrate-reduced GNPs with the AQ-Cyst complex. GNPs were functionalized on the basis of the following considerations: Firstly, chemical adsorption of normal thiol derivatives to the particle surface of GNPs (surface modification) occurs via Au-S bonding. Secondly, since the Au-S bond is very stable, the bonding of thiol group to GNPs helps in maintaining the stability of prepared composite after modification without the need for additional additives. Thirdly, the surface modification can be undertaken in an aqueous phase as it is soluble in water [52]. It is proposed that when GNPs are added to the AQ-Cyst complex, the thiol group of AQ-Cyst complex forms a covalent bond with GNPs after replacing citrate [53]. The interaction of citrate capped GNPs with AQ-Cyst complex is shown in scheme I. Here, CS is used as the dispersion matrix for AQ-Cyst complex capped GNPs.

### 3.3 Characterization of the prepared AQ-Cyst/GNPs nanocomposite:

#### 3.3.1 FTIR spectroscopy:

FTIR spectra of AQ-COOH shows a characteristic peaks at 1699 $\nu_{max}/cm^{-1}$ which is attributed to >C=O stretching vibration, $\nu_{max}/cm^{-1}$ 1590 due to C=C ring stretching vibration, peak $\nu_{max}/cm^{-1}$ 1438 due to –CH bending frequency and a broad peak also appears in the range of $\nu_{max}/cm^{-1}$ 3400- 3600 which is due to –OH stretching vibration of carboxylic acid group of AQ-COOH. An intense peak at $\nu_{max}/cm^{-1}$ 1281 is attributed to –C-O stretching frequency of AQ-COOH (Fig. 1 (I)). Following the interaction with cysteamine (Fig. 1 (II) curve a), a peak appears at $\nu_{max}/cm^{-1}$ 3397 which is due to –NH stretching vibration, the peak due to >C=O stretching is shifted to $\nu_{max}/cm^{-1}$1645 which is the characteristic peak for the amide linkage confirming the formation of AQ-Cyst composite. The peak at $\nu_{max}/cm^{-1}$ 1281 shifted to $\nu_{max}/cm^{-1}$ 1291 is due to the –CN aromatic stretching vibration while the peak at $\nu_{max}/cm^{-1}$ 2716 is assigned to –SH stretching vibration (Fig. 1 (II) curve a). After addition of GNPs to AQ-Cyst complex, the peaks due to thiol group (-SH) disappear Fig.1 (II) curve b). Hence, the FTIR spectroscopy suggests that AQ-COOH acid interacts with cysteamine to form AQ-Cyst complex via carbodiimide coupling and the formation AQ-Cyst/GNPs nanocomposite occur via gold thiol bonding.

#### 3.3.2 UV-Visible spectroscopy:

Fig.2 shows the UV-Visible spectra of AQ-Cyst/GNPs nanocomposite along with the other components of the system, namely the GNPs and AQ-COOH solutions. GNPs show an intense peak at $\lambda_{max}$(GNPs)/nm 520 which is attributed to surface plasmon response of prepared nanoparticles (curve a, photograph A). The UV-Visible spectrum shows three peaks at $\lambda_{max}$ (AQ-COOH)/nm 210, 258 and 335 (curve b). The $\lambda_{max}$(AQ-COOH)/nm at 258 is attributed to the $\pi$-$\pi^*$ transition of benzenoid system in AQ ring while the $\lambda_{max}$ (AQ-

COOH)/nm at 335 nm is due to the π-π* of quinoid system present in AQ-COOH molecule. The $\lambda_{max}$ (AQ-COOH)/nm at 210 have lower intensity compared to that at 258. This could be due to the blocking of carbonyl lone pair (curve b), so the $\lambda_{max}$ (AQ-COOH)/nm 210 is assigned to n-σ* transition as reported [54].

After carbodiimide coupling with cysteamine, no obvious change was observed in the UV-Visible spectrum of AQ-Cyst complex (data not shown). Following the interaction of the AQ-Cyst complex with GNPs (curve c, photograph C), a slight red shift was observed for the peak due to surface plasmon band of GNPs ($\lambda_{max}$ (GNPs)/nm 520 to 540), supporting the adsorption of AQ-Cyst complex on GNPs. From Fig. 2, it can be seen clearly that before the interaction, the AQ-Cyst complex was yellow but as the GNPs are added to the AQ-Cyst complex, a dark brown coloured precipitate of AQ-Cyst/GNPs nanocomposite forms, supporting the adsorption of AQ-Cyst complex to the GNPs.

**3.3.3 AFM characterization AQ-Cyst/GNPs/CS nanocomposite modified electrode film:**

Fig. 3 shows the AFM images of GCE following modification with CS (Fig. 3A), AQ-Cyst/CS (Fig. 3B) and AQ-Cyst/GNPs/CS (Fig. 3C) respectively. As can be seen from Fig. 3A, the CS modified GCE shows a uniform distribution of the polymer over the electrode while the AQ-Cyst/CS modified GCE shows a rough surface with a significant increase in the surface area. The figure also suggests that alignment of anthraquinone complex is vertical on the electrode. Although the surface area is improved the AQ-Cyst complex is not uniformly distributed in CS. Fig. 3 C displays AFM images of AQ-Cyst/GNPs/CS modified GC electrode, which indicates a further increase in the surface area of the AQ-Cyst/GNPs nanocomposite. The increased surface area is attributed to the effect of GNPs which might be due to an improved distribution and alignment of AQ-Cyst complex on GNPs, providing a very good environment for the improved distribution of AQ-Cyst/GNPs in CS.

### 3.4 Zeta potential characterization AQ-Cyst/GNPs/CS nanocomposite:

Zeta potential measurements provide an important criterion for the stability of a colloid system [55]. Stability of the AQ-Cyst/GNPs/CS nanocomposite was studied by re-dispersing and measuring the zeta potential of the prepared nanocomposite in aqueous medium. The zeta potential of citrate capped GNPs shows a zeta potential near -20 mV [56]. Upon adsorption of AQ-Cyst complex to GNPs, the zeta potential was found to be -39.5 mV as indicated in Supplementary Material III A. The shifting of zeta potential from -20 mV to -39.5 mV is attributed to the attachment of AQ-Cyst complex to GNPs. However, the zeta potential value of AQ-Cyst/GNPs nanocomposite after encapsulation within CS polymer was found to be as +45.5 mV (Supplementary Material III B). This result reveals the presence of positively charged CS molecules onto AQ-Cyst/GNPs nanocomposite surface that leads to an increase of zeta potential and also the high zeta potential value of AQ-Cyst/GNPs nanocomposite indicates stability of this nanocomposite [49].

### 3.5 Electrochemical characterization of AQ-Cyst/GNPs/CS nanocomposite:

Fig. 4 shows cyclic voltammograms of AQ-Cyst/GNPs/CS composite modified GCE in 0.1 M phosphate buffer solution (pH 6.5) as a function of scan rate (*v*, 10-300 mV/s). The figure shows positive and negative peaks corresponding to reduction and oxidation reaction respectively, attributed to the redox couple $AQ/AQH_2$ (Quinone to hydraquinone). The anodic peak potential, $E_a$ and cathodic peak potential, $E_c$ are -0.377 V and -0.490V respectively and the peak separation was found to be 113 mV at 10 mV/s scan rate showing that the process is close to a reversible system at slower scan rate and the rate of electron transfer is fast at electrode surface. Formal potential calculated from the mid-point of the cathodic and anodic peaks was found to be -0.433 V. According to the inset to Fig. 4, the peak current $i_p$ for oxidation and reduction increases with increasing scan rates and follows linear relationship

with the square root of scan rates [equations (1) and (2)], showing diffusion-controlled electrochemical reaction at the electrode surface.

$I_{pa}$ (A) [AQ-Cyst/GNPs/CS/GCE] = -0.06693 (A) -1.27911 A(s/mV) * [scan rates (mV/s)]

$R^2$= -0.99384, SD = 0.7707 (1)

$I_{pc}$ (A) [AQ-Cyst/GNPs/CS/GCE] = 2.59669 (A) + 1.71305A(s/mV) * [scan rates (mV/s)]

$R^2$= 0.99756, SD = 0.64827 (2)

We also studied the variation of peak current with scan rate i.e. $I_p$ vs (ν) as supplementary material (IV) which is also found to be linear indicating surface controlled process. Hence, for investigating the actual process occurring at electrode surface, a plot between log $i_p$ vs log ν was plotted and the slope of this plot was calculated (Fig. 6 A). Theoretically, slopes of 0.5 and 1 will be observed for pure diffusion and adsorbed species, respectively. However, a slope lying between 0.5 and 1 represents the mixed adsorption–diffusion controlled process, where the value indicates the level of contribution from the two components. Practically, the value of slope from 0.2–0.6 relates the process to be diffusion controlled, 0.60–0.75 for mixed diffusion–adsorption process and 0.75–1.0 for pure adsorption processes, respectively [57]. In this study, the slope of log $I_p$ vs log ν has been found to be 0.39 and 0.45 for oxidation and reduction processes respectively, suggesting the electrochemical process is mainly governed by diffusion.

To compare the effect of each component, we also prepared CS/GCE, AQ-COOH/CS/GCE, AQ-Cyst/CS/GCE and the result have been investigated in phosphate buffer (0.1M, pH 6.5) using cyclic voltammetry (supplementary material V). The cyclic voltammogram of CS/GCE showed no redox peaks (curve a), while a redox couple has been observed for AQ-COOH/CS/GCE (curve b), AQ-Cyst/CS/GCE (curve c) and AQ-Cyst/GNPs/CS/GCE (curve d), with peak separations of 132, 188 and 113 mV at the scan rate of 10 mV/s, respectively, which clearly shows improved electrochemistry and facile electron transfer for the AQ-

Cyst/GNPs/CS/GCE in the presence of gold nanoparticles compared to the other electrodes. The values of α and $k_s$ were calculated to be 0.56 and 4.764 $s^{-1}$ for AQ-Cyst/GNPs/CS/GCE using Laviron's equation. The values of α and $k_s$ were also calculated by Laviron's plot for AQ-COOH/CS/GCE and AQ-Cyst/CS/GCE (data not shown) and the results are compared in Table 1. The data show that in AQ-Cyst/GNPs/CS nanocomposite modified GCE, GNPs takes part in enhancing the electron transfer of redox pair at the electrode and hence participates in improved kinetics of AQ-Cyst/GNPs/CS nanocomposite compared to AQ-Cyst/CS and AQ-COOH/CS modified GCE. It is proposed that AQ-Cyst complex interacts with GNPs via covalent bonding (Au-SH) leading to the formation of a more stable nanocomposite than AQ-Cyst and AQ-COOH which increases the surface area of electrode resulting in high current density (curve d , supplementary material V).

According to Laviron's equation, the relationship between peak current (Ip) and surface coverage can be described as:

$$I_p = (n^2F^2 / 4RT)\, \nu\, A\, \Gamma^* \quad \ldots\ldots (6)$$

where Γ* is the surface coverage of the redox species and ν being the potential sweep rate and taking average of both cathodic and anodic results, Γ* value of around 12.64 x $10^{-9}$ mol $cm^{-2}$ was derived indicating more than a monolayer of electroactive species upon the electrode surface.

### 3.6. Electrocatalytic reduction of oxygen on the AQ-Cyst/GNPs/CS nanocomposite modified GCE:

Fig. 6 displays the electrocatalytic reduction of oxygen on AQ-Cyst/GNPs/CS nanocomposite modified GCE in the absence (curve a) and presence (curve b-f) of different concentrations (1.25, 1.84, 2.05, 2.25, 2.5 mg/ L) of $O_2$ at the scan rate of 10 mV $s^{-1}$. A large increase in the reduction current after the addition of different concentrations of oxygen along with a

decrease in oxidation current shows the electrocatalytic reduction of oxygen using the modified electrode. It has already been reported [58] that the reduction of $O_2$ on carbon surface takes place either by $O_2/O_2^-$ reaction at equilibrium followed by disproportionation of the superoxide anion or to a slow chemical step following the first electron transfer where reaction step two is rate determining step. However, the electrochemical behaviour of carbon materials is affected by electrode pre-treatment and oxidation which increases the $O_2$ reduction rate due to electrocatalysis by oxygen containing surface species. In the present case it is proposed that by the use of anthraquinone derivative based nanocomposite, semiquinone intermediate is formed in the reduction of quinones and due presence of these quinone moieties on carbon surface the nanocomposite shows high chemical reactivity towards $O_2$ reduction [45] as represented in scheme 2.

The peak for oxygen reduction was observed at -0.80 V at bare GCE and the current observed was 3 µA (result not shown). The reduction of oxygen at nanocomposite modified electrode occurred at -0.53 V (*cf.* Fig. 6, Inset I). The use of AQ-Cyst functionalized GNPs results in improving the current density by increasing the surface area and also results in improved film forming properties like better film adhesion, avoids leaching of redox mediator anthraquinone derivative from the electrode surface. The simultaneous use of anthraquinone derivative along with GNPs not only decreases the operating potential for oxygen reduction but also improves the electron transfer over the electrode surface [59]. The obtained data was used to plot a calibration curve (Inset II to Fig.6); which shows the reduction peak current increased linearly until the dissolved oxygen concentration reached 5.8 mg $L^{-1}$ with the linear equation I (µA) = 4.2681 [$O_2$(mg $L^{-1}$)] – 3.1957 and correlation coefficient ($R^2$) of 0.9959. Further, upon increasing the concentration of dissolved oxygen over 5.84 mg $L^{-1}$, the curve deviates from linearity (data not discussed as beyond the scope of this paper). The detection limit was found to be 0.03 mg $L^{-1}$ at signal to noise ratio of 3 which

has been compared with other reported works in Table 2 [60-68] which indicated prepared electrode gives rise to electroanalytical improvements over most other reported works. The work is in progress for preparation of screen-printed electrode for this work and a patent has been applied for the prepared material [69].

### 3.7 Performance of sensor:

The stability of the electrode was studied electrochemically by using cyclic voltammetry. To study the stability of AQ-Cyst/GNPs/CS modified GC electrode, 25 repeated cycles were scanned but no appreciable change was observed in the cyclic voltammogram of the modified electrode which justifies the stability of present nanocomposite modified GC electrode. When 25 continuous cycles scan were carried out at 20 mV/s scan rate, 5.2% decrease of the initial response at 2.48 mg $L^{-1}$ oxygen was observed. The RSD of 2.2% was observed for three successive measurements of one nanocomposite modified electrode at 2.48 mg $L^{-1}$ oxygen indicating good reproducibility of the proposed dissolved oxygen sensor. The long term stability of the proposed sensor was also studied. Lifetime was more than 4-5 months when the electrode was kept at 4°C, when not in use. The response of the dissolved oxygen was also tested time to time. During the first 3 days, the response current showed about 6% decrease.

### 3.8 Real sample analysis:

To study the performance of the sensor for the real samples by using AQ-Cyst/GNPs/CS modified GC, we collected pond water from BHU and studied the presence of dissolved oxygen in pond water by using standard addition method and the results are shown in Table 3. The results obtained confirm the suitability of the present modified electrode as sensor.

## 4. Conclusions

A nanocomposite material using AQ-COOH/Cysteamine capped GNPs which act as reinforcement element and chitosan which acts as a matrix material for the nanocomposite has been prepared. Further, this AQ-Cyst/GNPs/CS nanocomposite has been used as the dissolved oxygen sensor successfully. The simultaneous use of anthraquinone derivative along with GNPs not only decreases the operating potential for oxygen reduction but also improves the electron transfer over the electrode surface.

## 5. Acknowledgement:

The present work has been performed by funds sanctioned by DBT, India and UGC-UKIERI Thematic Partnerships. The authors are grateful for this financial support.

**Reference:**


1. S. Bose, T. Kuila, A. K. Mishra, R. Rajasekar, N. H. Kim, J. H. LeeDOI: 10.1039/C1JM14468E (Feature Article) *J. Mater. Chem.*, 2012, **22**, 767-78
2. K. Friedrich, S. Fakirov, Z. Zhang, in Polymer Composites: From Nano- to Macro-Scale Springer Science+ business media, Inc., 233, spring street, NewYork, USA, 2005, pp. 367.
3. S. Mandal, D. Roy, R. V. Chaudhari, M. Sastry, *Chem. of Mat.*, 2004, **16**, 3714–3724.
4. S. Guo, E. Wang, *Anal. Chim. Acta* 2007,**598**, 181–192.
5. M.H. Rashid, R.R. Bhattacharjee, A. Kotal, T.K. Mandal, *Langmuir*, 2006, **22**, 7141-7146.
6. F. Hoppe-Seiler, *"Ueber chitosan und zellulose," Berichte der Deutschen Chemischen Gesellschaft*, 1894,**27**, 3329–3331.
7. S. H. Chiou, W. T. Wu, *Biomat.,* 2004, **25**, 197–204.
8. S.Parvez, M. M. Rahman, M. A. Khan, M. Anwar H. Khan,J. M. M. Islam, M. Ahmed, M. F. Rahman, B. Ahmed, *Polymer Bulletin*, 2012, **69**, 715-731.
9. M. Darder, M. Colilla, E. R. Hitzky, *Applied Clay Science*, 2005, **28**, 199–208.
10. M. R. Tarasevich, A. Sadkowski, E. Yeager, *in Comprehensive Treatise of Electrochemistry, ed B. E. Conway, J. O. M. Bockris, E. Yeager, S. U. M. Khan and R. E. White, New York: Plenum Press*; 1983, **7**, 301–398.
11. B. Sˇ ljukic, C. E. Banks, R. G. Compton, *J. Iran Chem. Soc.,* 2005, **2**, 1–25.
12. R. Ramamoorthy, P. K. Dutta, S. A. Akbar, *J. Mat. Sci.,* 2003, **38**, 4271 – 4282.
13. I. Kruusenberg, N. Alexeyeva, K. Tammeveski, *Carbon*., 2009, **47**, 651 –658.
14. J. P. Collman, P. Denisevich, Y. Konai, M. Marrocco, C. Koval, F. C. Anson, *J. Am. Chem. Soc.,* 1980, **102**, 6027-6036.
15. C. Shi, B. Steiger, M. Yuasa, F. C. Anson, *Inorg. Chem.*, 1997, **36**, 4294-4295.
16. K. Vaik, A. Sarapuu, K. Tammeveski, F. Mirkhalaf, D. J. Schiffrin, *J. Electroanal. Chem.*, 2004, **564**, 159–166.
17. X. Li, A. A. Gewirth, *J. Am. Chem. Soc.,* 2005, **127**, 5252-5260.

18. N. Mano, J. L. Fernandez, Y. Kim, W. Shin, A. J. Bard, A. Heller, *J. Am. Chem. Soc.*, 2003, **125**, 15290-15291.

19. V. Soukharev, N. Mano, A. Heller, *J. Am. Chem. Soc.*, 2004, **126**, 8368-8369.

20. M. S. E. Deab, T. Ohsaka, *Angew. Chem. Int. Ed.,* 2006, **45**, 5963-5966.

21. H. Ye, R. M. Crooks, *J. Am. Chem. Soc.*, 2005, **127,** 4930-4934.

22. L. Hutton, M. E. Newton, P. R. Unwin, J. V. Macpherson, *Anal. Chem.*, 2009, **81**, 1023–1032.

23. K. Gong, P. Yu, L. Su, S. Xiong, L. Mao, *J. Phys. Chem. C*, 2007, **111,** 1882-1887.

24. N. Alexeyeva, K. Tammeveski, *Anal. Chim. Acta*, 2008, **618**, 140–146.

25. H. Park, T. G. Kwon, D. S. Park, Y. B. Shim, *Bull. Korean Chem. Soc.*, 2006, **27**, 1763-1768.

26. E. D. Jeong, M. S. Won, Y. B. Shim, *Bull. Korean Chem. Soc.*, 1998, **19**, 417-422.

27. P. Manisankar, A. Gomathi, *Electroanal.,* 2003, **15**, 1051-1057.

28. M. Shourian, H. Ghourchian, *Sens. Actuat. B,* 2010, **145**, 607–612

29. N. Mogharrab, H. Ghourchian, *Electrochem. Comm.,* 2005, **7**, 466–471.

30. G. Maia, F. C. Maschion, S. T. Tanimoto, K. Vaik, U. Mäeorg, K. Tammeveski, *J. Solid State Electrochem.,* 2007, **11,** 1411–1420.

31. M. Kullapere, K. Tammeveski, *Electrochem. Comm.,* 2007, **9**, 1196–1201.

32. M. W. Lehmann, D. H. Evans, *J. Electroanal. Chem.,* 2001, **500**, 12–20.

33. M. Shamshipur, A. Salami, S. M. Golabi, H. Sharghi, M. F. Mousavi, *J. Solid State Electrochem.*, 2001, **5**, 68-73.

34. A. Huisssoud, P. Tissot, *J. Appl. Electrochem.,* 1998, **28**, 653-657.

35. A. Salimi, C. E. Banks, R. G. Compton, *Phys. Chem. Chem. Phys.,* 2003, **5**, 3988–3993.

36. T. Wilson, J. Zhang, C. C. Oloman, D. D. M. Wayner, *Int. J. Electrochem. Sci.,* 2006, **1**, 99-109.

37. M. Kullaperea, J. M. Seinberga, U. Mäeorga, G. Maia, D. J. Schiffrin, K. Tammeveski, *Electrochimi. Acta.,* 2009, **54**, 1961–1969.

38. P. Manisankar A. Gomathi, D. Velayutham, *J. Solid State Electrochem.,* 2005, **9**, 601–608.

39. A. A. Abdelwahab, O. S. Jung, Y. B. Shim, *J. Electroanal. Chem.*, 2009, **632**, 102–108.

40. A. Sarapuu, K. Vaik, D. J. Schiffrin, K. Tammeveski, *J. Electroanal. Chem.,* 2003, **541**, 23-29.

41. K. Vaik, U. Maeorg, F. C. Maschion, G. Maiac, D. J. Schiffrin, K. Tammeveski, *Electrochim. Acta*, 2005, **50**, 5126–5131

42. F. Mirkhalaf, K. Tammeveski, D. J. Schiffrin, *Phys. Chem. Chem. Phys.*, 2004, **6**, 1321–1327.

43. N. Alexeyeva, T. Laaksonen, K. Kontturi, F. Mirkhalaf, D. J. Schiffrin, K. Tammeveski, *Electrochem. Commun.*, 2006, **8**, 1475–1480.

44. A. Sarapuu, K. Helstein, K. Vaik, D. J. Schiffrin, Kaido Tammeveski, *Electrochim. Acta*, 2010, **55**, 6376–6382.

45. G. Jurmann, D. J. Schiffrin, K. Tammeveski, *Electrochim. Acta.,* 2007, **53**, 390–399.

46. I. Tiwari, M. Singh, M. Gupta, S. K. Aggarwal, *Mat. Res. Bull.,* 2012, **47**, 1697–1703.

47. C. E. Banks, G. G. Wildgoose, C. G. R. Heald, R.G. Compton, *J. Iran. Chem. Soc.,* 2005, **2**, 60-64.

48. I. Tiwari, M. Gupta, *Mat. Res. Bull.,* 2014, **49**, 94-101.

49. A. Sharma, C. M. Pandey, G. Sumana, U. Soni, S. Sapra, A. K. Srivastava, T. Chatterjee, B. D. Malhotra, *Biosen. Bioelectron.,* 2012, **38**, 107–113.

50. S. S. Wong, in Chemistry of protein conjugation and cross-linking. ed. Boca Raton, CRC Press; 1991. Ch. 6, pp. 195-9.

51. S. Sam, L. Touahir, J. S. Andresa, P. Allongue, J. N. Chazalviel, A. C. G. Laemmel, C. H. D. Villeneuve, A. Moraillon, F. Ozanam, N. Gabouze, S. Djebbar, *Langmuir*., 2010, **26**, 809–814.

52. M. Giersig, P. Mulvaney, *Langmuir.,* 1993, **9**, 3408-3413.

53. S. Y. Lin, Y. T. Tsai, C. C. Chen, C. M. Lin, C. Chen, *J. Phys. Chem. B*., 2004, **108**, 2134-2139.

54. M. S. El Ezaby, T. M. Salem, A.H. Zewail, R.Issa, *J. Chem.Soc.B.,* 1970, **7**, 1293-1296.

55. R. J. Hunter, Zeta potential in colloid science: principles and application, London; New York: Academic Press, 1981.

56. Z. Wang, M. Li, Y. Zhang, J. Yuan, Y. Shen, L. Niu, A. Ivaska, *Carbon*., 2007, **45**, 2111–2115.

57. I. Tiwari, M. Gupta, P. Sinha, S. K. Aggarwal, *Electrochim. Acta.,* 2012, **76**, 106-111.

58. K. Tammeveski, K.S. Kontturi, R.J. Nichols, R.J. Potter, D.J. Schiffrin, *J. Electroanal. Chem*., 2001, 515, 101–112.

59. H. Ryoo, Y. Kim, J. Lee, W. Shin, N. Myung, H. G. Hong, *Bull. Korean Chem. Soc.*, 2006, **27**, 672-678.

60. T. H. Tsai, C. Y. Yang, S. M. Chen, *Int. J. Electrochem. Sci.,* 2013, **8**, 5250 – 5261.

61. T. H. Tsai, S. H. Wang, S. M. Chen, *Int. J. Electrochem. Sci.,* 2011, **6**, 1655 – 1668.

62. R. C. S. Luz, F. S. Damos, A. A. Tanaka, L. T. Kubota, *Sens. Actuat. B.,* 2006, **114**, 1019–1027.

63. J. C. Duartea, R. C. S. Luz, Flavio, F. S. Damos, A. A. Tanaka, L. T. Kubota, *Anal. Chim. Acta.,* 2008, **612**, 29–36.

64. B. Haghighi, S. Bozorgzadeh, *Anal. Chim. Acta.*, 2011, **697**, 90–97.

65. E. S. Ribeiro, S. L. P. Dias, Y. Gushikem, L. T. Kubota, *Electrochim. Acta*., 2004, **49**, 829–834.

66. M. S. P. Francisco, W. S. Cardoso, Y. Gushikem, *J. Electroanal. Chem.,* 2005, **574**, 291–297.

67. R. J. Zheng, Y. M. Fang, S. F. Qin, J. Song, A. H. Wu, J. J. Sun, *Sens. Actuat. B.,* 2011, **157**, 488– 493

68. Y. Xiong, J. Xu, D. Q. Zhu, C. F. Duan, Y. F. Guan, *J. Sol-Gel Sci. Technol.*, 2010, **53**, 441–447.

69. I. Tiwari, M. Singh, R. Prakash, Patent No. 3150/DEL/2013 dated 23.10.2013

**Figure Captions:**

**Fig.1**. FTIR spectra of AQ-COOH (I); AQ-Cyst complex (II, curve a); AQ-Cyst/GNPs (II, curve b) nanocomposite

**Fig.2**. UV-Visible spectra of GNPs (curve a); AQ-COOH (curve b); AQ-Cyst/GNPs nanocomposite (curve c)

**Fig.3**. Atomic Force Microscopic images of glassy carbon electrode after modification with chitosan (A), AQ-Cyst/CS (B) and AQ-Cyst/GNPs/CS (C) AQ-Cyst/GNPs/CS.

**Fig.4**. Cyclic voltammogram of AQ-Cyst/GNPs/CS composite modified glassy carbon electrode in 0.1 M phosphate buffer solution (pH 6.5) at different of scan rates (ν, 10-300 mV/s); **Inset:** Randles-Sevcik plot.

**Fig.5**. **(A)** Plot between log $i_p$ vs log ν **(B)** Laviron's plot (Ep vs log scan rates) at AQ-Cyst/GNPs/CS/GCE.

**Fig.6**. Electrocatalytic reduction of oxygen on AQ-Cyst/GNPs/CS nanocomposite modified GCE in the absence (curve a) and presence of different concentration (1.25, 1.84, 2.05, 2.25, 2.5 mg $L^{-1}$) of $O_2$ (curve b-f); **Inset:** (I) Differential pulse voltammogram for oxygen reduction on AQ-Cyst/GNPs/CS nanocomposite modified electrode in presence of (a) 1.84 mg $L^{-1}$ and (b) 2.5 mg $L^{-1}$ of oxygen at -0.53 V vs. Ag/AgCl; (II) Calibration plot (Peak current $i_p$ vs [$O_2$ (mg $L^{-1}$)].

**Scheme I**: Interaction of citrate capped GNPs to AQ-Cyst complex.

**Scheme II:** Reaction taking place at AQ-Cyst/GNPs/CS/GC electrode surface

**Supplementary Material I:** (A) TEM image of gold nanoparticles, Inset: TEM of gold nanoparticle at low magnification (B) diffraction pattern of gold nanoparticles

**Supplementary material II**: Optimization of GNPs concentration

**Supplementary material III A**: Zeta potential measurement of AQ-Cyst/GNPs nanocomposite in aqueous solution.

**Supplementary material III B**: Zeta potential measurement of AQ-Cyst/GNPs/CS nanocomposite in aqueous solution.

**Supplementary material IV**: Variation of peak current with scan rates i.e. $I_p$ vs (ν) at the AQ-Cyst/GNPs/CS nanocomposite modified GCE.

**Supplementary material V**: Cyclic voltammograms of different modified electrodes; CS/GC (curve a), AQ-COOH/CS/GC (curve b), AQ-Cyst/CS/GC (curve c), AQ-Cyst/GNPs/CS/GC (curve d) electrode in phosphate buffer (0.1 M, pH 6.5).

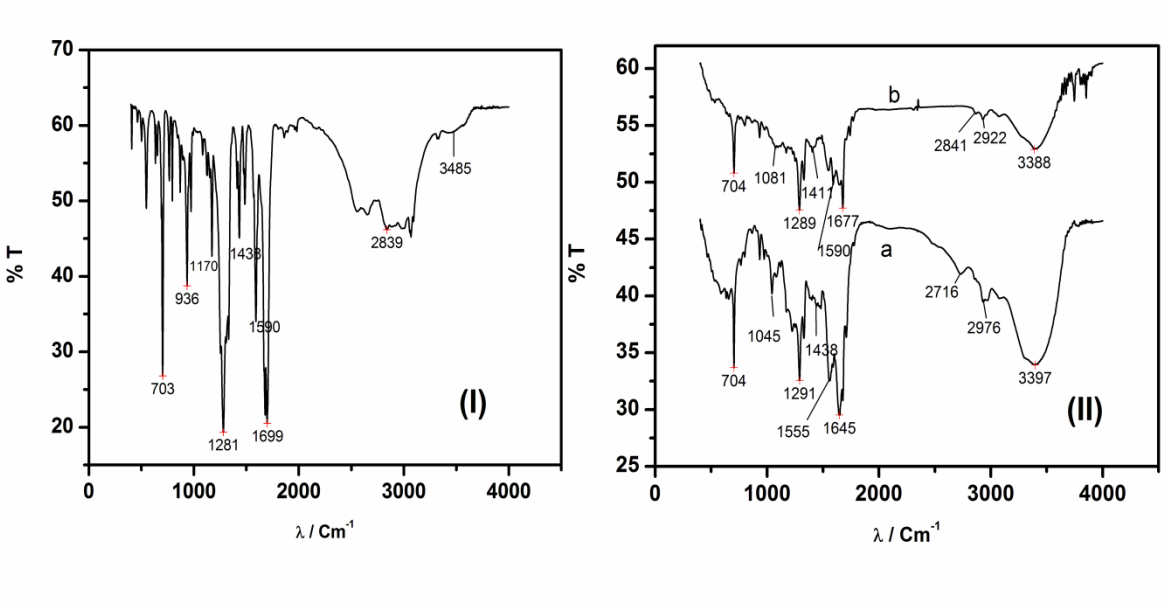


**Fig. 1**

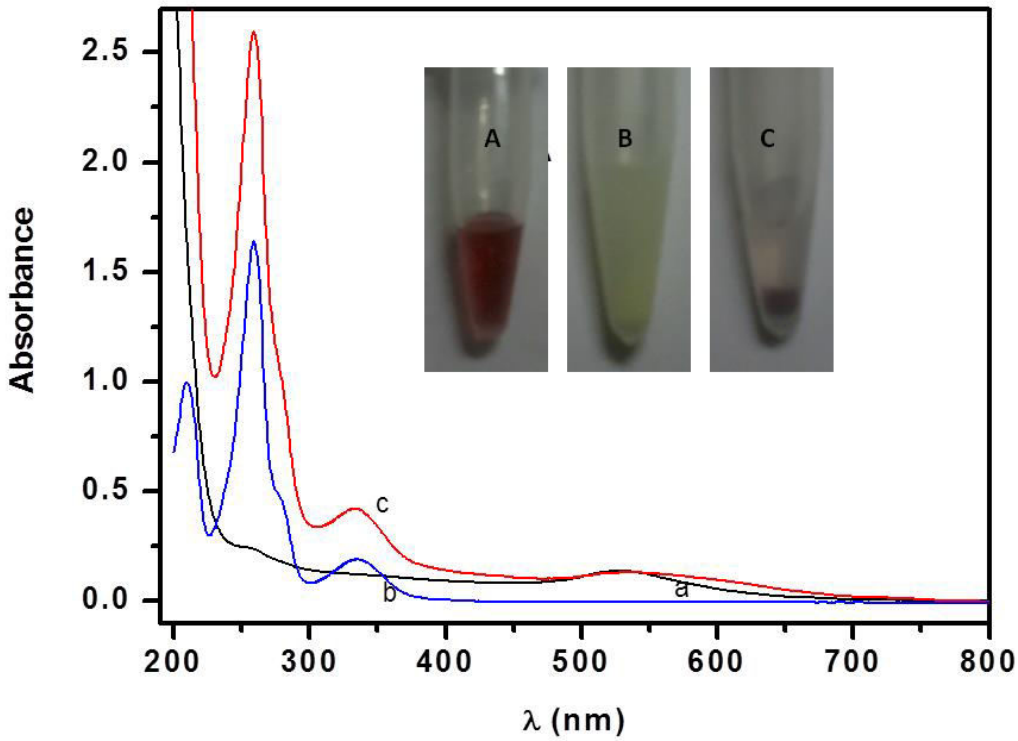


**Fig. 2**

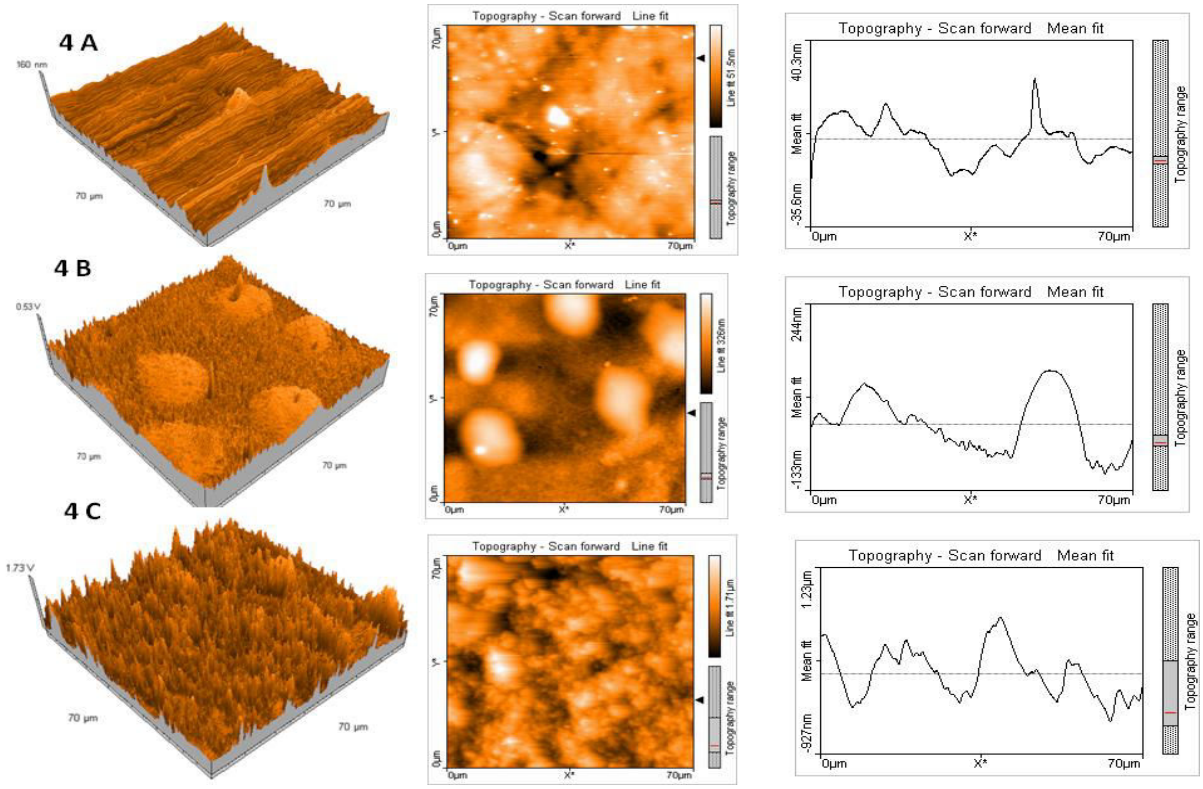


**Fig. 3**

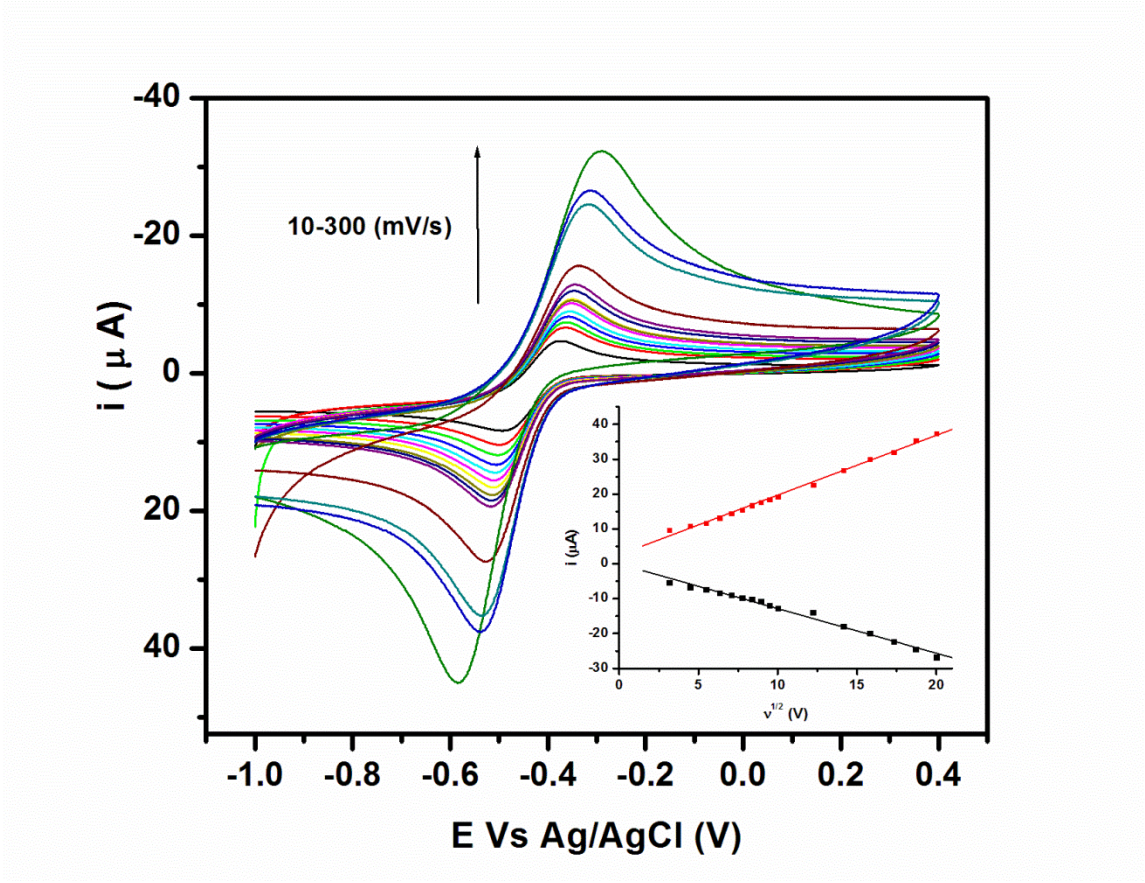


**Fig. 4**

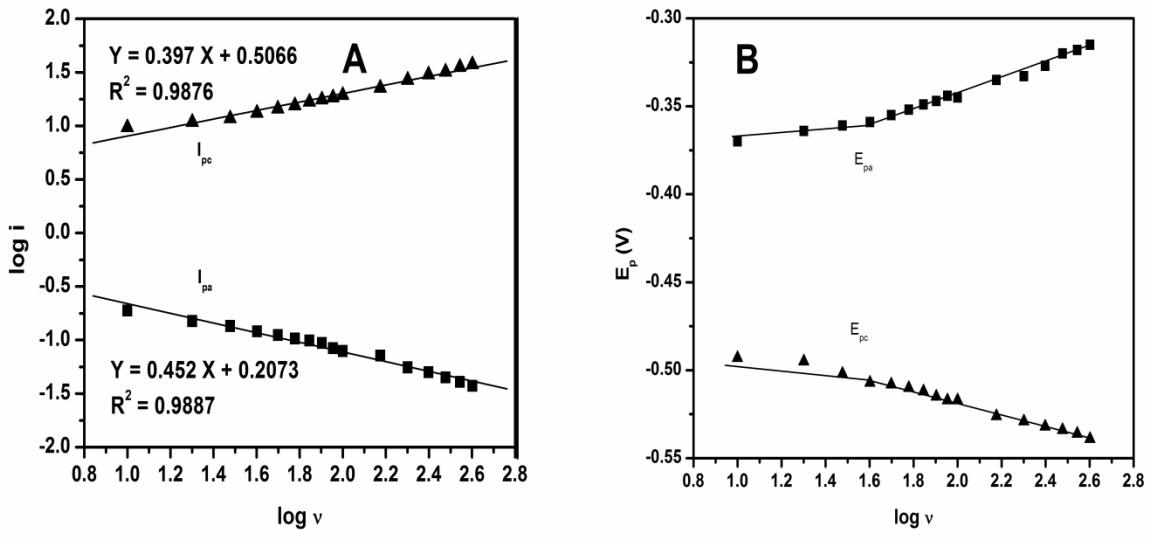


Fig. 5

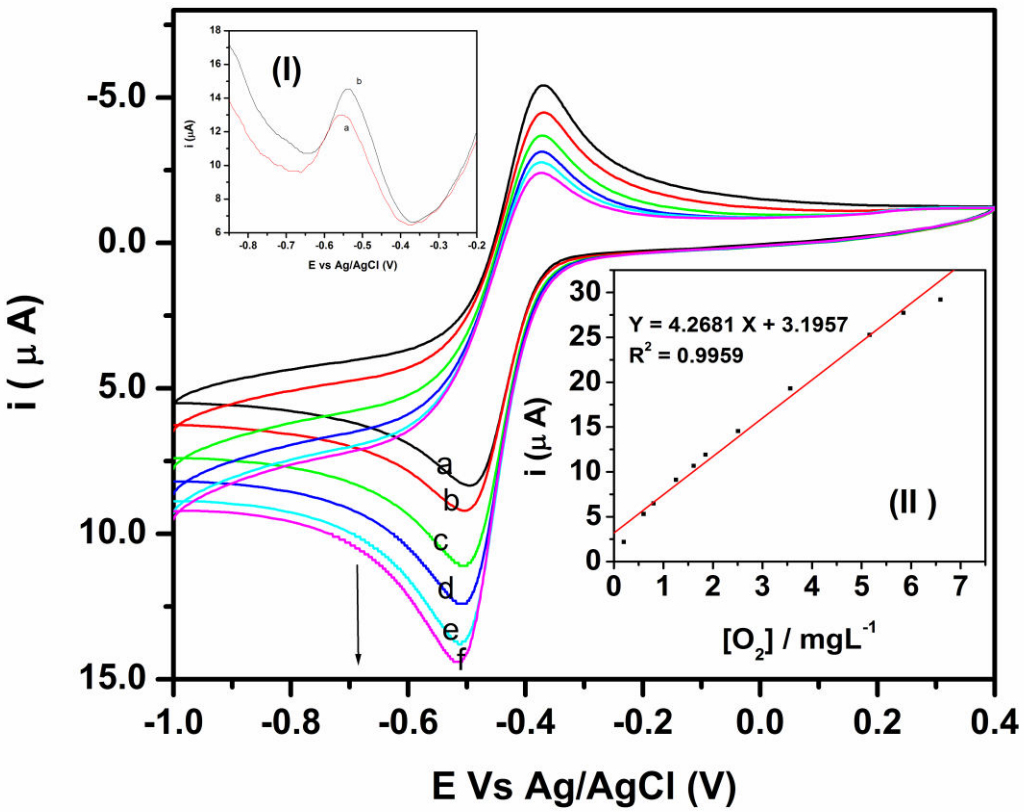


Fig. 6

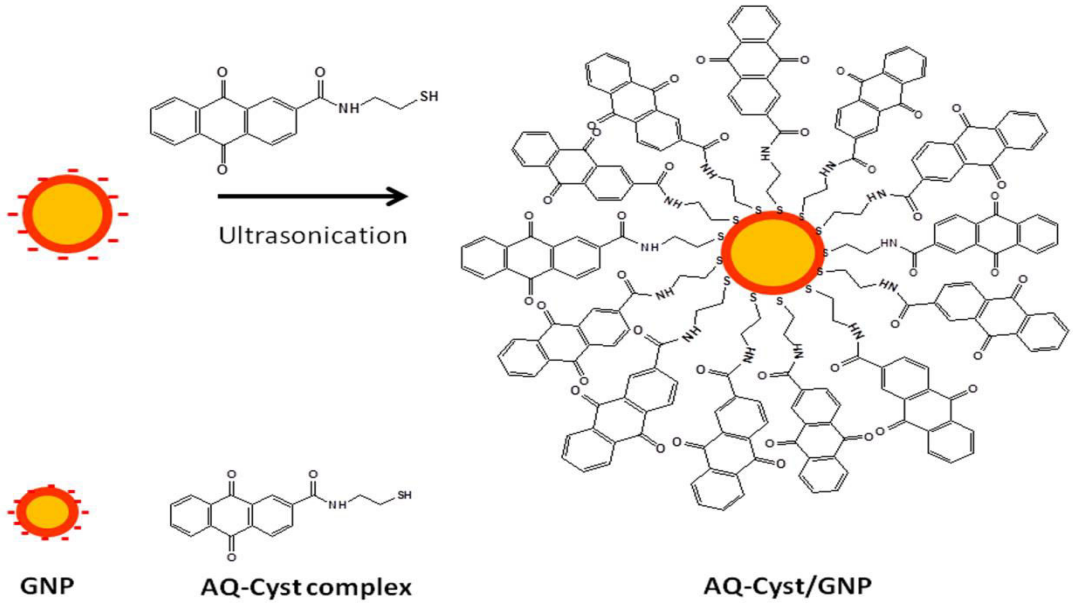


**Scheme I**

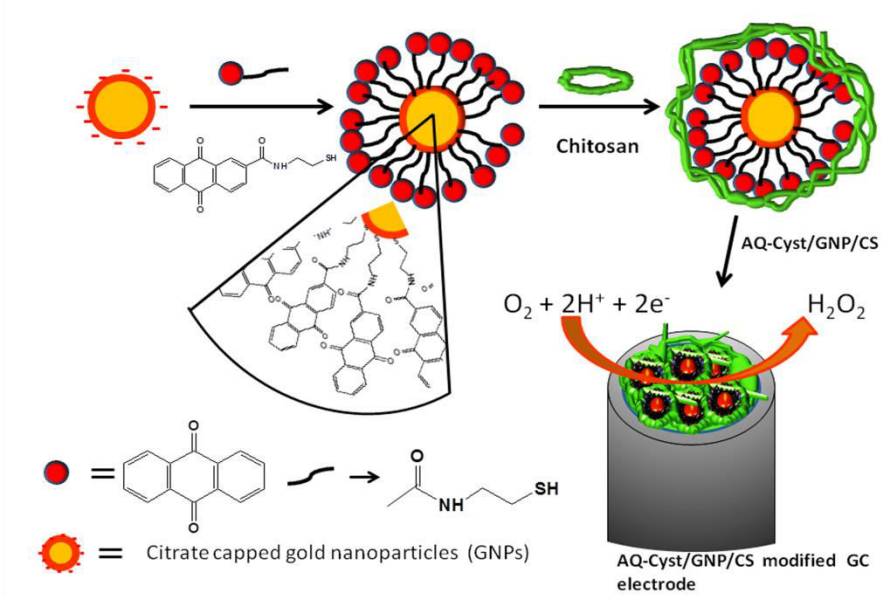


**Scheme II**

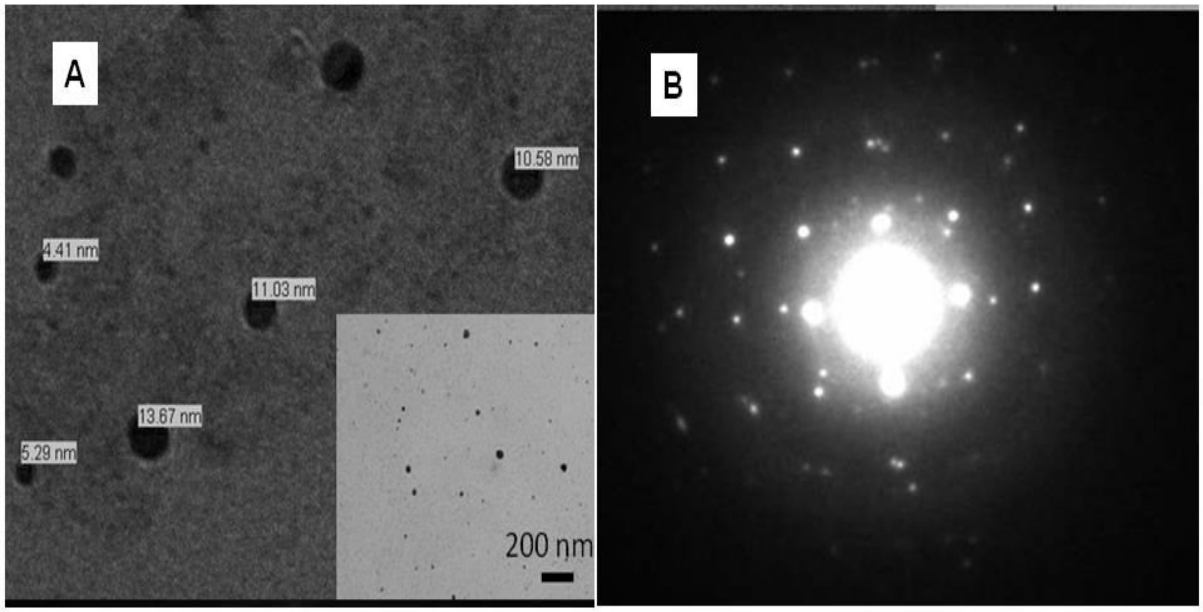


**Supplementary material I**

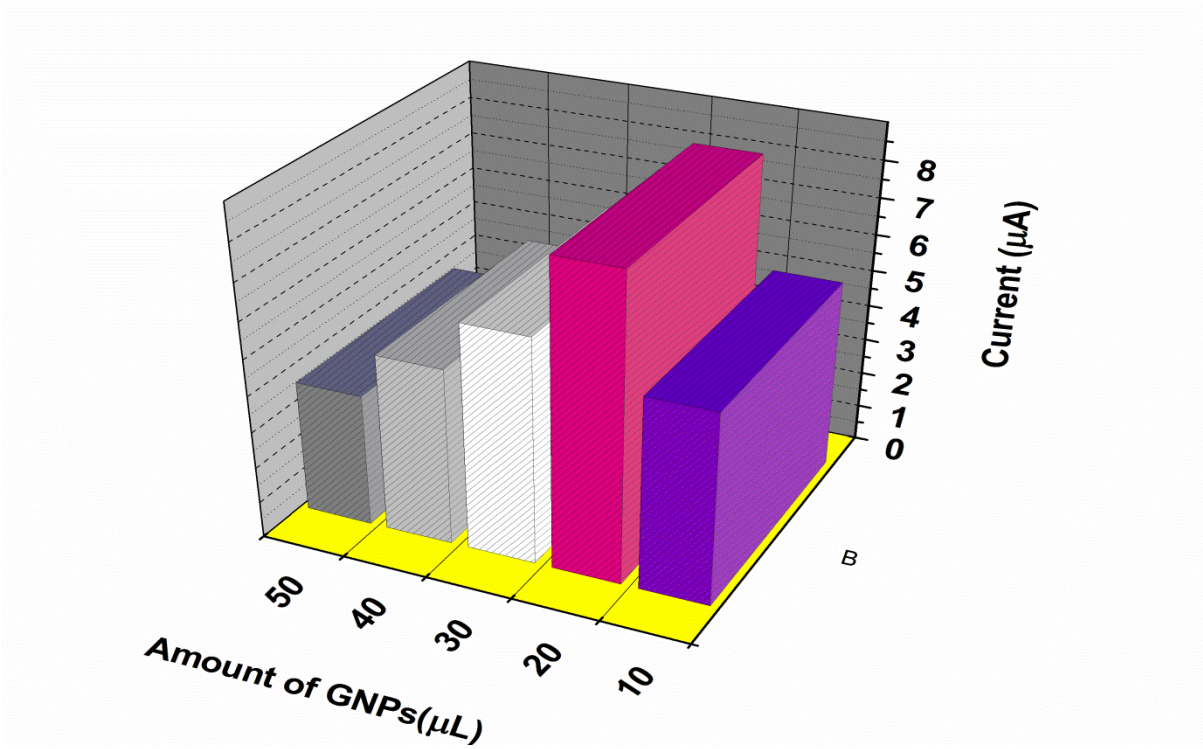


**Supplementary material II**

| | | Mean (mV) | Area (%) | Width (mV) |
|---|---|---|---|---|
| Zeta Potential (mV): 45.5 | Peak 1: | 45.6 | 98.9 | 7.23 |
| Zeta Deviation (mV): 7.52 | Peak 2: | 19.4 | 1.1 | 1.88 |
| Conductivity (mS/cm): 0.326 | Peak 3: | 0.00 | 0.0 | 0.00 |

Result quality : Good

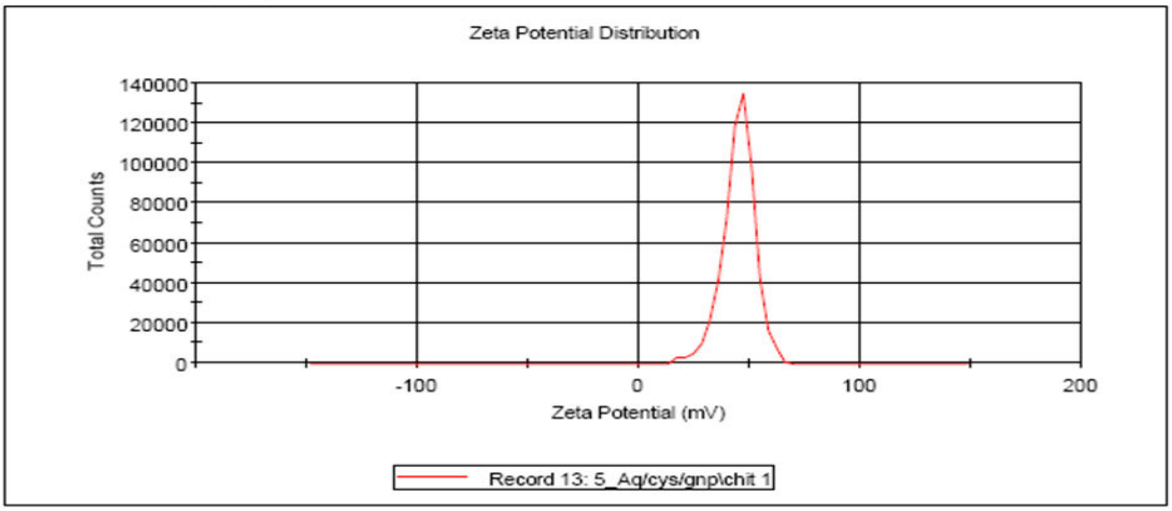


**Supplementary material III A**

| | | Mean (mV) | Area (%) | Width (mV) |
|---|---|---|---|---|
| Zeta Potential (mV): -39.5 | Peak 1: | -39.5 | 100.0 | 7.22 |
| Zeta Deviation (mV): 7.22 | Peak 2: | 0.00 | 0.0 | 0.00 |
| Conductivity (mS/cm): 0.114 | Peak 3: | 0.00 | 0.0 | 0.00 |

Result quality : Good

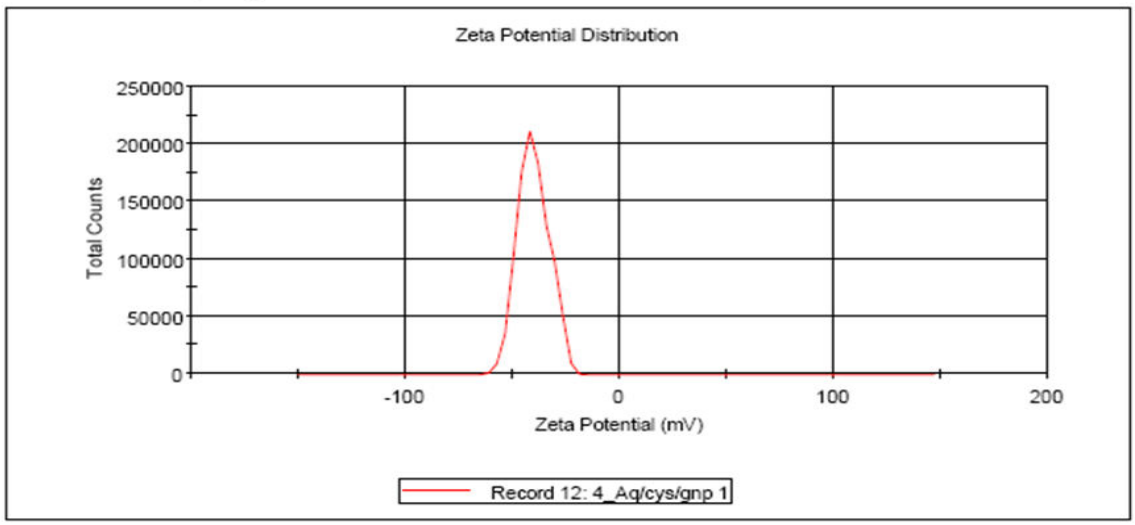


**Supplementary material III B**

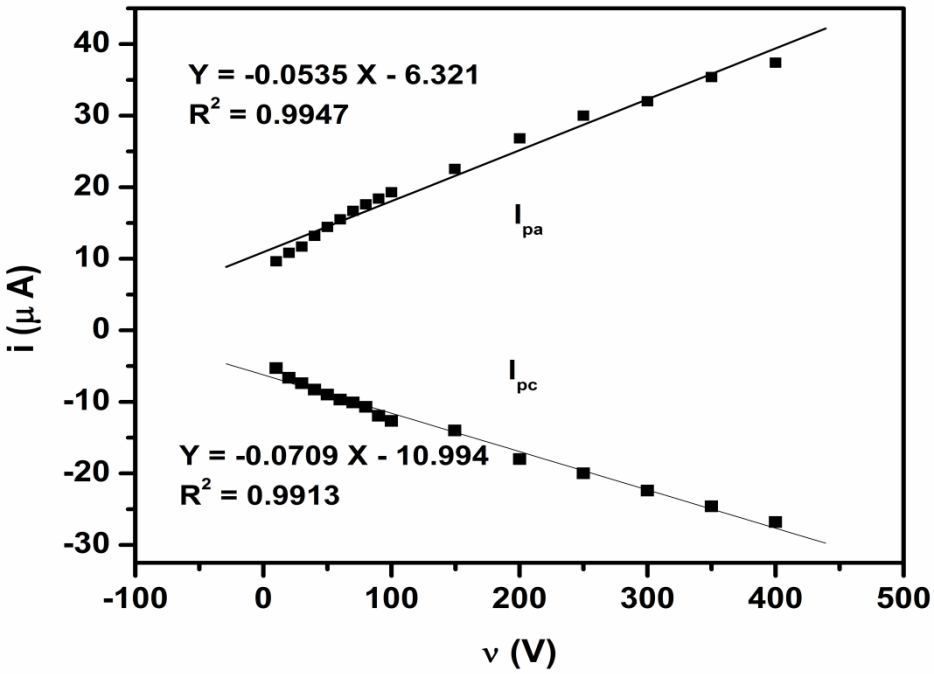


**Supplementary material IV**

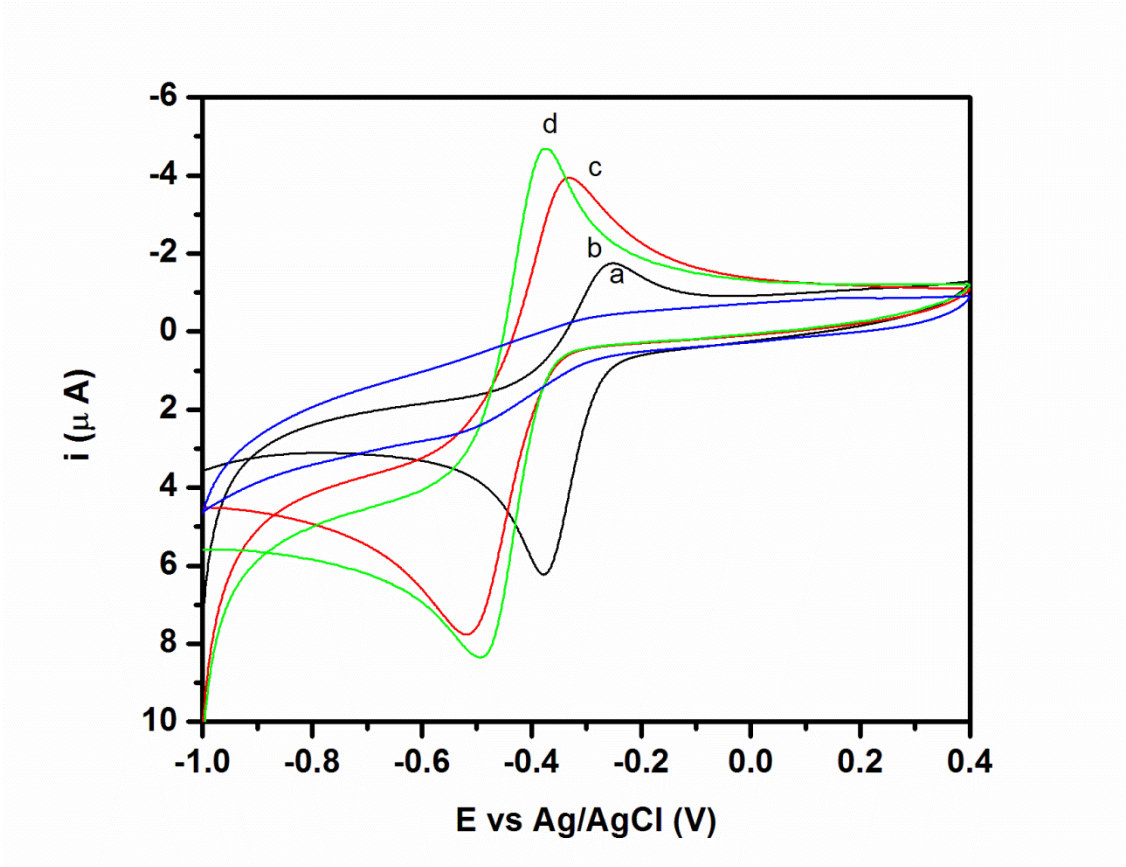


**Supplementary material V**

Table 1: Kinetic parameters for the fabricated electrodes:

| Sl No. | Electrodes | Electron transfer Coefficient (α) | Charge transfer rate constants, $K_s$ ($S^{-1}$) | Surface coverage area (mol $cm^{-2}$) |
|---|---|---|---|---|
| 1. | AQ-Cys/GNPs/CS | 0.56 | 4.764 | $12.47 \times 10^{-9}$ |
| 2. | AQ-Cys/CS | 0.61 | 1.446 | $2.92 \times 10^{-10}$ |
| 3. | AQ-2-COOH/CS | 0.73 | 0.709 | $4.18 \times 10^{-10}$ |

Table 2: Comparison of linear range and detection limit of some modified electrode and AQ-Cyst/GNPs/CS nanocomposite modified glassy carbon electrode for the dissolved oxygen sensor

| Serial no. | Type of sensor construction | Technique | Linear range (mg $L^{-1}$) | Detection limits (mg $L^{-1}$) | References |
|---|---|---|---|---|---|
| 1. | GNP-*f*-CNT/ GCE | RDE | 0 – 50 | 0.1 | [60] |
| 2. | AQDS/PLL-GA/GCE | RDE | 0.7- 4.4 | 0.3 | [61] |
| 3. | CoTSPc/PLL /GCE | Chronoamperometry<br>DPV | 0.2-8<br>0.2-8 | 0.096<br>0.072 | [62] |
| 4. | FeTsPc/FeT4MPyP | | 0.2 -6.4 | 0.06 | [63] |
| 5. | nanoPd-MWCNTs/GCE | ECL | 0.08-0.94 (mM) | 0.02 (mM) | [64] |
| 6. | SiSb/CoTmPyP/CPE | Chronoamperometry | 1.0 - 12.8 | - | [65] |
| 7. | $SiO_2/Nb_2O_5$/CPE | Chronoamperometry | 1.0 - 13.6 | - | [66] |
| 8. | CdS-SPCEs | ECL | 1.7-33 | 0.02 | [67] |
| 9. | $Ru(bpy)_3^{2+}$-doped xerogel solutions based on TMOS, MTMS and TFP–TriMOS, | Fiber optic | - | 0.03 | [68] |
| 10. | AQ-Cyst/GNPs/CS | CV | 0.2-5.8 | 0.03 | Present work |

Table 3: Determination of dissolved oxygen in water samples by the AQ-Cyst/GNPs/CS nanocomposite modified GC electrode and Winkler's method

| Sample Name | AQ-Cyst/GNPs/CS nanocomposite modified GC (ppm) | Winkler's method (ppm) |
|---|---|---|
| Pond water | 3.8(±0. 30)(n=4) | 4.1 (±0.30)(n=4) |